

Article

A High-Throughput Imagery Protocol to Predict Functionality upon Fractality of Carbon-Capturing Biointerfaces

Bruno Rafael de Almeida Moreira ^{*,†}, Armando Lopes de Brito Filho [†], Marcelo Rodrigues Barbosa Júnior [†] 
and Rouverson Pereira da Silva 

Department of Engineering and Mathematical Sciences, School of Agricultural and Veterinarian Sciences, São Paulo State University (Unesp), Jaboticabal, São Paulo 14884-900, Brazil; armando.brito@unesp.br (A.L.d.B.F.); marcelo.junior@unesp.br (M.R.B.J.); rouverson.silva@unesp.br (R.P.d.S.)

* Correspondence: b.moreira@unesp.br

† These authors contributed equally to this work.

Abstract: Surface quality is key for any adsorbent to have an effective adsorption. Because analyzing an adsorbent can be costly, we established an imagery protocol to determine adsorption robustly yet simply. To validate our hypothesis of whether stereomicroscopy, superpixel segmentation and fractal theory consist of an exceptional merger for high-throughput predictive analytics, we developed carbon-capturing biointerfaces by pelletizing hydrochars of sugarcane bagasse, pinewood sawdust, peanut pod hull, wheat straw, and peaty compost. The apochromatic stereomicroscopy captured outstanding micrographs of biointerfaces. Hence, it enabled the segmenting algorithm to distinguish between rough and smooth microstructural stresses by chromatic similarity and topological proximity. The box-counting algorithm then adequately determined the fractal dimension of microcracks, merely as a result of processing segments of the image, without any computational unfeasibility. The larger the fractal pattern, the more loss of functional gas-binding sites, namely N and S, and thus the potential sorption significantly decreases from 10.85 to 7.20 mmol CO₂ g⁻¹ at sigmoid Gompertz function. Our insights into analyzing fractal carbon-capturing biointerfaces provide forward knowledge of particular relevance to progress in the field's prominence in bringing high-throughput methods into implementation to study adsorption towards upgrading carbon capture and storage (CCS) and carbon capture and utilization (CCU).

Keywords: adsorbent; box-counting method; high-resolution stereomicroscopy imagery data; physical adsorption; porous carbonaceous material; simple linear iterative clustering algorithm; superpixel segmentation



Citation: Moreira, B.R.d.A.; Brito Filho, A.L.d.; Barbosa Júnior, M.R.; Silva, R.P.d. A High-Throughput Imagery Protocol to Predict Functionality upon Fractality of Carbon-Capturing Biointerfaces. *Agronomy* **2022**, *12*, 446. <https://doi.org/10.3390/agronomy12020446>

Academic Editor: Silvia Arazuri

Received: 26 December 2021

Accepted: 5 February 2022

Published: 10 February 2022

Publisher's Note: MDPI stays neutral with regard to jurisdictional claims in published maps and institutional affiliations.



Copyright: © 2022 by the authors. Licensee MDPI, Basel, Switzerland. This article is an open access article distributed under the terms and conditions of the Creative Commons Attribution (CC BY) license (<https://creativecommons.org/licenses/by/4.0/>).

1. Introduction

The IPCC's experts estimate the Earth's surface temperature at 2 °C above the preindustrial baseline (1850–1900) by 2100. Therefore, stakeholders (e.g., the scientific community, policymakers, and civil community) must be aware of the commitment, cooperation and coordination they need to elaborate on if they are to effectively mitigate global warming and prevent planetary collapse over the coming years [1]. Numerous CCU and CCS platforms exist for reducing emission of CO₂. The literature focuses on absorption [2–4], adsorption, cryogenic distillation [5], and separation [6]. Particularly the adsorption works on the simplest physical principles of capturing and binding an adsorbate in pores and functional sites on the surface of the material [7]. Adsorption, relative to absorption on amine-containing solutions, is not energy-intensive and other immediate advantages refer to compactness and conservation of space, and a wider range of suitable scaffoldings and powders to assemble resilient sorbents [8]. The application of carbon-capturing materials is common in coal-firing and gas-firing power stations across the USA, UK and European Union. They can potentially prevent the industry from emitting about 10,000.00 Mt

CO₂ yearly [9]. Precisely, an effective adsorption can remove 85% of the adsorbate out of the flue-gas consisting of 10–15% CO₂ [9]. However, screening out materials for the purpose of full-scale adsorption can be costly via traditional methodologies, such as adsorption/desorption isotherm [10]. Thus, development of an alternative is imperative to level-up cost-effectiveness of the technology and progress in the field's prominence in bringing CCU and CCS into implementation at a global scale. As adsorbers are often irregular on the surface, an option to analyze them cost-effectively would be an imagery protocol consisting of fractal analysis.

Fractal is the power-law of self-similarity [11]. The theory fundamentally describes anything in nature consisting of similar copies of itself at multiple scales and dimensions, ranging from 2 to 3 [12]. The closer to 2 the D_F , the smoother the geometric pattern. By contrast, the closer from 3 the D_F the rougher and more complex the geometric pattern [13]. Therefore, fractal analytics consists of applying non-traditional mathematics to solve non-Euclidean geometries [14]. It proves useful to analyze adsorption both quantitatively and qualitatively by seamlessly modelling features of a topographically irregular surface [15,16]. However, if there is any structural dependency in the dataset, it becomes rather obsolete and thus we may need to approach multifractal analysis [12]. Multifractal analysis handles both accuracy and comprehensiveness. Hence, it can compensate for the non-ability of single fractal analysis to adequately characterize a material for dynamic pore-filling phenomena [12]. For instance, a multifractal model can predict either for distribution of pores upon crushing or adsorption of CH₄ on coal with greater precision than possible with the probabilistic functions, namely Gandin–Schumann, Rosin–Rammler and Logit [12]. It provides an overview of the impact of adsorption on the surface's functionality and resilience. If an adsorbate suddenly penetrates through the structure, it destabilizes the adsorber, making it incapable of capturing cost-effectively. By contrast, underperformance is not likely from a gradual adsorption-desorption [12].

The contemporary academic literature about applying fractals to adsorption focuses on fossil resources, such as coal, coalbed methane and shale. By contrast, research and technological development in micro and mesoporous biosurfaces is at an embryonic stage (Figure S1, Supplementary Material). For instance, an original study by Zhang et al. [17] provides a consistent reference of the robustness of fractal numerical simulation in generating data to model a non-Darcy flow in tortuous capillary tubes and decide whether an inorganic porous matrix is feasible to store supercritical CO₂. The fractal model, namely Frankel–Halsey–Hill, can predict a functional relationship between adsorption and porosity of a structurally complex and changeable shale [18]. The larger the fractal pore, the more probable the material is to perform an effective adsorption. Furthermore, Zhang et al. [19] on the adsorption of NO_x from flue-gas on sludge char, picture the importance of pore's fractality to the dynamic physical processes of capturing and binding. Most notably, they elaborate how work-up conditions can impact adsorption both negatively and positively. While the pyrolytic residence time does not influence the dimensional features of pore network, such as diameter, width and volume, the temperature can structure-up larger and more complex physical gas-adsorbing sites measurable from an isothermal sorption analyzer.

Numerous analytical protocols exist for determining fractality, for characterization and understanding how it could impact the adsorption. The literature focuses on adsorption/desorption isotherm, AFM [13], photogrammetric reconstruction from SEM [20], mercury intrusion porosimetry, X-ray diffraction, SAXS, SANS, micrographs, and adsorption desulfurization with an auxiliary microwave irradiation [21]. For instance, AFM [13] and SEM [20] can directly measure irregularities on the surface. However, both can limit the field of view to 100 μm and, eventually, make the project costly and complex rather than easy-to-setup, besides the requirement of an expert for accuracy and reliability. FESEM, EDS and adsorption/desorption isotherm are an exceptional merger for analyzing pore's morphology and how it impacts the structuration and function of an adsorbing coal [22]. However, the integrative protocol by the authors [22] needs processing micrographs in the

photogrammetric environment of Image-Pro Plus. The software works on imagery data (2D and 3D). However, addressable and programmable functions such as adjusting size and resolution, cropping and editing specific areas, rotating, adding filters, and balancing often are not available from the open-source version. Another disadvantage refers to the need of polishing samples by an Ar-ion milling system with an accelerating voltage of 6 keV to improve image's quality and resolution, making it time-consuming and energy-intensive. Complementarily, another software capable of processing fractal imagery data is MATLAB [23]. The multi-paradigm program supports direct uploads from cameras, scanners, disks or CD-ROM. However, the professional version is private.

An imagery protocol by Ren et al. [24] can determine functional relationships between fractal dimensions of microstructures and relative mechanical stresses on the surface of bituminous coal. It is effective and can process data in real time. However, it can be costly by demanding a universal testing machine, state-of-the-art microcomputer and high-speed camera (~50 FPS) to capture digital images on the material during uniaxial loading at 5 mm min^{-1} . Furthermore, the methodology by Lin et al. [25] can predict on BCM for the porosity and how it can impact the adsorption on fractal deep shale with atomic-level precision. The BCM determines the D_F by covering the pattern with boxes then counting the number of boxes touching about it. Graphically, D_F is the slope of the curve by plotting the N_s on the y-axis against the s on the x-axis. N_s and s stand as the number and size of boxes, respectively [26]. Therefore, the steeper the curve, the more fractal the object. By contrast, the flatter the curve, the less fractal the object, as the degree of details does not increase with reducing the box's size. BCM works on a 2D plane by iteratively generating smaller boxes of finer grids until the process achieves the accuracy we might expect on an optimal processing of digital images. Thus, the magnitude of D_F ranges from 1 for perfectly smooth geometry to 2 for extremely rough geometry. By shrinking the box's size, we can more accurately capture the pattern. However, if there are any unpredictable low-level properties in the image, BCM becomes rather complex, making it incapable of determining fractality without computational unfeasibility. An option to improve programmatically determining D_F on BCM would be SLIC. SLIC can segment an image into superpixels by chromatic similarity and topological proximity. It can massively generate pixels merely as a result of 'k-mean' discretization, so it is likely to prevent BCM from underperformance.

Therefore, in light of research and innovation in applying fractal analysis to adsorption, we elaborated stereomicroscopy, superpixel segmentation and box-counting algorithm into a high-throughput imagery protocol to predict adsorption at microstructural stress. A secondary objective was to analyze if it could be feasible for integrating hydrothermal carbonization and pelletization into a system for making agricultural, agro-industrial and forestry residues into high-throughput carbon-capturing biointerfaces towards progressing on eco-compatible adsorption and waste management.

2. Materials and Methods

2.1. Origination of Scaffoldings in Carbon-Capturing Biointerfaces

Sources of powders for making carbon-capturing biointerfaces via an integrative carbonization-pelletization system included agricultural, agro-industrial and forestry residues from full-scale sugar-energy mill plant, timber-processing factory, mechanical harvesting and pilot-scale mushroom-growing house (Table 1). Materials were dried at $125 \text{ }^\circ\text{C}$ into a constant mass, milled and sieved to 0.25–0.45 mm, then characterized in triplicate to moisture (ASTM E871–82), volatile matter (ASTM E871–82), fixed-carbon (ASTM E871–82), ash (ASTM D1102–84), C, H, O, N, and S (EN 15104, EN 15289) in elemental analyzer (Perkin-Elmer: Waltham, MA, USA, 2400 Series II CHNS/O), and calorific value in an isotherm calorimeter bomb (C 200, IKA-Werke GmbH & Co. KG: Staufen, Germany), as per the methods in Iftikhar et al. [27].

Table 1. Origination and physicochemical properties scaffoldings for making carbon-capturing biointerfaces.

Biointerface	Material	Source	Moisture	V _M	F _C	Ash	C	H	O	N	S	HHV
I	Sugarcane bagasse	Full-scale sugar-energy mill plant	12.40	77.35	14.20	8.45	46.70	10.20	42.95	0.10	0.05	19.75
II	Pinewood sawdust	Full-scale timber processing factory	11.40	79.80	11.70	8.50	45.20	14.85	39.80	0.10	0.05	21.40
III	Peanut pod hull	Mechanical harvesting	71.90	62.90	6.00	31.10	50.20	2.80	46.75	0.15	0.10	15.30
IV	Paddy straw	Pilot-scale production of <i>Pleurotus ostreatus</i>	72.20	61.50	9.35	29.15	38.40	13.40	48.10	0.05	0.05	14.45
V	Peaty compost	Pilot-scale production of <i>Agaricus subrufescens</i>	74.55	59.05	8.65	32.30	54.10	0.60	44.90	0.20	0.20	16.10

V_M, volatile matter; F_C, fixed-carbon; HHV; higher heating value.

2.2. Pilot-Scaling Manufacturing of Carbon-Capturing Biointerfaces

2.2.1. Thermochemical Pre-Treatment

The hydrothermal carbonization (HTC) was carried out in vertical autoclaving reactor (Table S1, Supplementary Material) for ten standard batches. A batch consisted of 15 kg powdery material as the solid phase for every 150 L de-ionized water as the catalytical liquid phase, as per the method by Sharma and Dubey [28]. After introducing the load, the equipment was sealed and programmed to 2 h HTC at 200 °C; heating ramp was set to 1.5 °C min⁻¹ to a gradual thermochemical pre-treatment, with N₂ injected continuously through an automatic gas pump to expel the oxygen inside and consolidate a continuous and porous carbon matrix. The auto-generated pressure inside the reactor was 1.5 MPa. After the process leveled off, the equipment was turned off, the pressure valve released and the fraction of hydrochar was recovered, cooled to room temperature in cold water to prevent further coalification. The hydrochar was then filtered through a cellulose-nitrate membrane to remove impurities, heated at 105 °C into constant mass and stored dry in an airtight receptacle for sampling for pelletization.

2.2.2. Pressing

The protocol of compaction started with introducing 1.5 kg hydrochar into the silo of the assembly of pelleting. The presser machine (Table S2, Supplementary Material) was then set and controlled at 200 MPa and 125 °C [29] to properly densify the material into market-grade pellets (Ø = 7 mm). After grinding, the pelletizer automatically ejected the pellets out of the compressing channel (flat die) directly onto the vibratory screener, and then the conveyor moved them to the storing unit at the end of the process. Samples were cooled to room temperature then stored dry in 2 kg airtight bags in the laboratory until quantitative analysis.

2.3. Assessing Potential Adsorption on Biointerfaces

To quantitatively analyze the impact of material on the ability of the biointerface to capture and bind CO₂ in pores and functional sites on the surface, key-variables to adsorption were determined as follows:

The static adsorption of CO₂ [μ, mmol g⁻¹] was determined by thermogravimetric analyzer (PerkinElmer, Waltham, MA, USA); representative samples of 0.1 g in triplicate were loaded onto the platinum pan and the temperature was raised from 25 to 200 °C, heating ramp and flow rate of 10 °C min⁻¹ and 50 mL min⁻¹, respectively. After the samples were outgassed to drive moisture off, the temperature was decreased to 25 °C to measure the adsorption on the surface; on the complete saturation, the CO₂ was switched to pure N₂, and the temperature was increased to 200 °C to analyze the desorption. The adsorption-desorption cycle was repeated ten times at 1 MPa [30].

Surface area [S_A, m² g⁻¹], and diameter [D_P, nm] and width [W_P, nm] of pore were determined by Brunauer–Emmett–Teller equation (Equation (1)) and Barrett–Joyner–Halenda method, respectively, from data on adsorption-desorption of N₂ on samples of 0.1 g in

triplicate in an isothermal sorption analyzer (Q5000 SA, Waters: Milford, MA, USA) at 77 K [31].

$$\frac{1}{V_a \left(\frac{P_0}{P} - 1 \right)} = \frac{C - 1}{V_m C} \times \frac{P}{P_0} + \frac{1}{V_m C} \quad (1)$$

where P was the partial pressure of adsorbate gas in equilibrium with the surface, Pa; P_0 was the saturated pressure of adsorbate gas, Pa; V_a and V_m were the volumes of gas adsorbed at STP and to produce an apparent monolayer on the surface, mL; and C was the dimensionless constant of enthalpic adsorption on the powdery sample.

Volume of pore [V_P , $\text{m}^3 \text{g}^{-1}$] was also determined from isotherms of N_2 -sorption on samples of 0.1 g in triplicate, previously vacuum outgassed at 200 °C for 6 h to remove gases or vapors [31].

Durability [D , %]: The ability for the pellet to resist shocks and collisions was tested in 100 g samples in triplicate in a custom-made rotating chamber at 50 rpm for 10 min; after the mechanical trial, the material was sieved then weighted to quantify the durable and non-durable (particles finer than 3.25 mm) fractions as per the method in Abdulmumini et al. [32].

Hygroscopicity [H_{yg} , %]: The H_{yg} was determined through the ratio of mass of 100 g samples in triplicate before and after two weeks of storage in a chamber at a relative humidity of $62.25 \pm 1.50\%$ and temperature of 41.05 ± 0.70 °C, as per the method in Abdulmumini et al. [32].

Functionality at the surface: To complete analysis and establish an eventual relationship between fractality and functionality, an EDS was carried out on biointerfaces to determine O, N and S at 20 keV for high-resolution scanning [33].

2.4. Setting-Up Imagery Protocol

2.4.1. Stereomicroscopy

Representative samples of one-hundred random pellets per biointerface were photographed in an apochromatic stereo microscope (ZEISS Stemi-305, Carl Zeiss, Oberkochen, Germany) at $20\times$ magnification to maximize the field of view and acquire 18 mm objects. The scanning was performed in a routine work lab in a dark room to prevent light from damaging images and thus ensure outstanding contrast and color accuracy. Cylindric pellets were placed horizontally on the plate then 90° flipped to capture the whole surface through interchangeable confocal objective lenses and thus gather sufficient details on low-level regions for photogrammetric reconstruction of fractality from complete micrographs without cropping, rotating, balancing, filtering or any other clever feature for adjusting files. Pixel intensity was programmatically extracted from snapshots of 8 bits in the environment of ZEN software then imported as an Excel file or notepad extension to computationally determine the D_F of microcracks. Snapshots were saved as PNG, which is a raster-graphic format file supporting lossless data compression and compatible with soft computing.

2.4.2. Superpixel Segmentation and Box-Counting

To computationally determine the D_F (Equation (2)) of mechanical stresses on biointerfaces upon micrographs, we first performed an oversegmentation with SLIC algorithm to group images into superpixels by color similarity and topological proximity merely as a result of processing low-intensity regions in the CIELAB space. The BCM was then applied to sub-graphs which carry more information than pixels and align better with edges than rectangular patches. To photogrammetrically reconstruct the biointerfaces' surface into line charts, fractal superpixels were quantized and organized in histograms by intensity, and then the frequency of observations was normalized between 1 and 2 to refer the thresholds of BCM for smoothness and roughness, respectively.

$$D_F = \lim_{\delta \rightarrow \infty} \frac{\ln(N_s)}{\ln(s)} \quad (2)$$

where N_S was the number of boxes necessary to completely cover the pattern, and s was the box size [34].

2.5. Data Analysis

A box-plot diagram was elaborated to compare biointerfaces by fractality. To predict functionality upon fractality, sigmoid Gompertz function (Equation (3)) was fitted to data, starting parameterization with $\alpha = 10$, $\beta = 1$ and $k = 0.10$ [35]; its adequacy was analyzed on adjusted coefficient of determination (r_{adj}^2). Spearman correlation was measured between independent variables. Another method of applying explanatory statistics included PCA to orthogonalize the high-dimensionality original dataset into useful latent hits with eigenvalues equal to 1 or greater by KMO test [36]. All analyses were carried out in the environment of R-project for statistical computing and graphics [37].

$$f_x = \alpha e^{-\beta e^{-kx}} \quad (3)$$

where f_x was the dependent variable; x was the independent variable; α was the asymptote; β was the infection point; κ was the slope coefficient, and e was the Euler constant.

3. Results

3.1. Fractality of Biointerfaces

Apochromatic stereomicroscopy enabled us to capture outstanding snapshots on bio-surfaces (Figure 1). We required 45–60 min to process a single sample of one-hundred pellets. The SLIC algorithm segmented the micrographs into k -connected superpixels merely as a result of processing low-intensity regions in the image by color similarity and topological proximity. Its computational power and robustness towards discretization generated sufficient information for pixel-wise quantization of derivative site-specific RGB microarrays by intensity of color or hue. Hence, superpixel oversegmentation enabled the BCM to accurately capture the D_F of microstructural stresses on biosurfaces and photogrammetrically reconstruct them by the fractality (Figure 2).

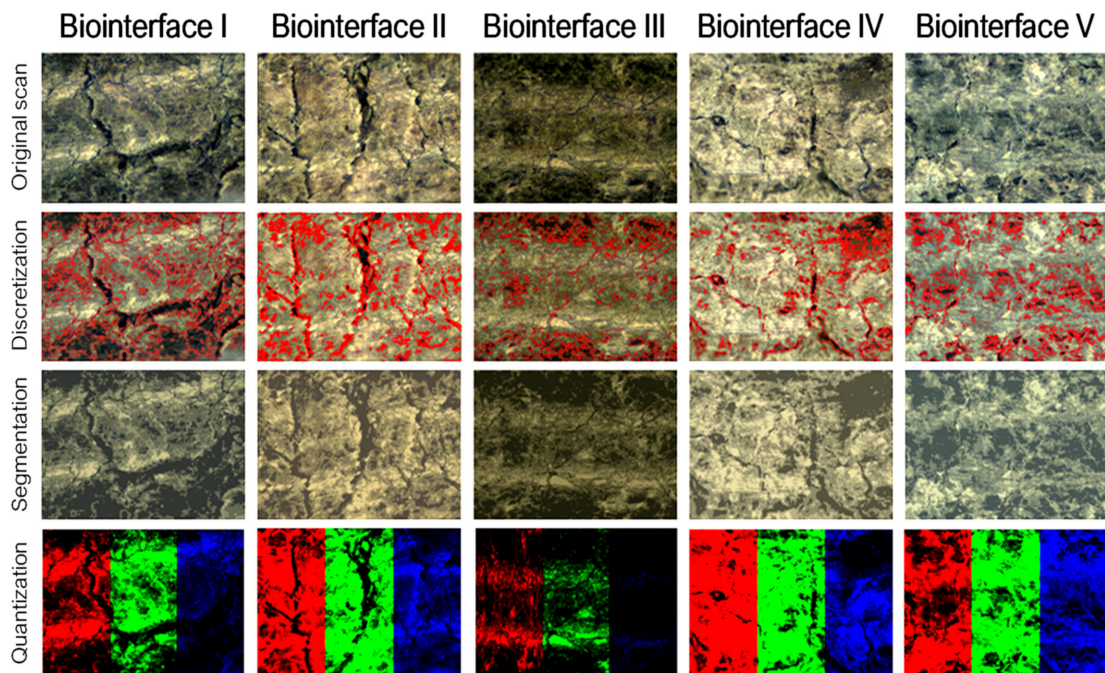


Figure 1. Computational processing of micrographs on fractal carbon-capturing biointerfaces from hydrochars of sugarcane bagasse (I), pinewood sawdust (II), peanut pod hull (III), wheat straw (IV) and peaty compost (V). The outcome of apochromatic stereomicroscopy, namely original scan, becomes

the input for segmentation. The SLIC algorithm then discretizes between rough and smooth regions on the digital surface merely as a result of processing low-intensity properties in the 2D plane. The next step of the protocol is to measure the intensity of k-mean pixel-wise segments of an image (RGB quantization, range 0–255) for determination of D_F on box-counting algorithm and photogrammetric reconstruction of fractality into a descriptive diagram (box-plot).

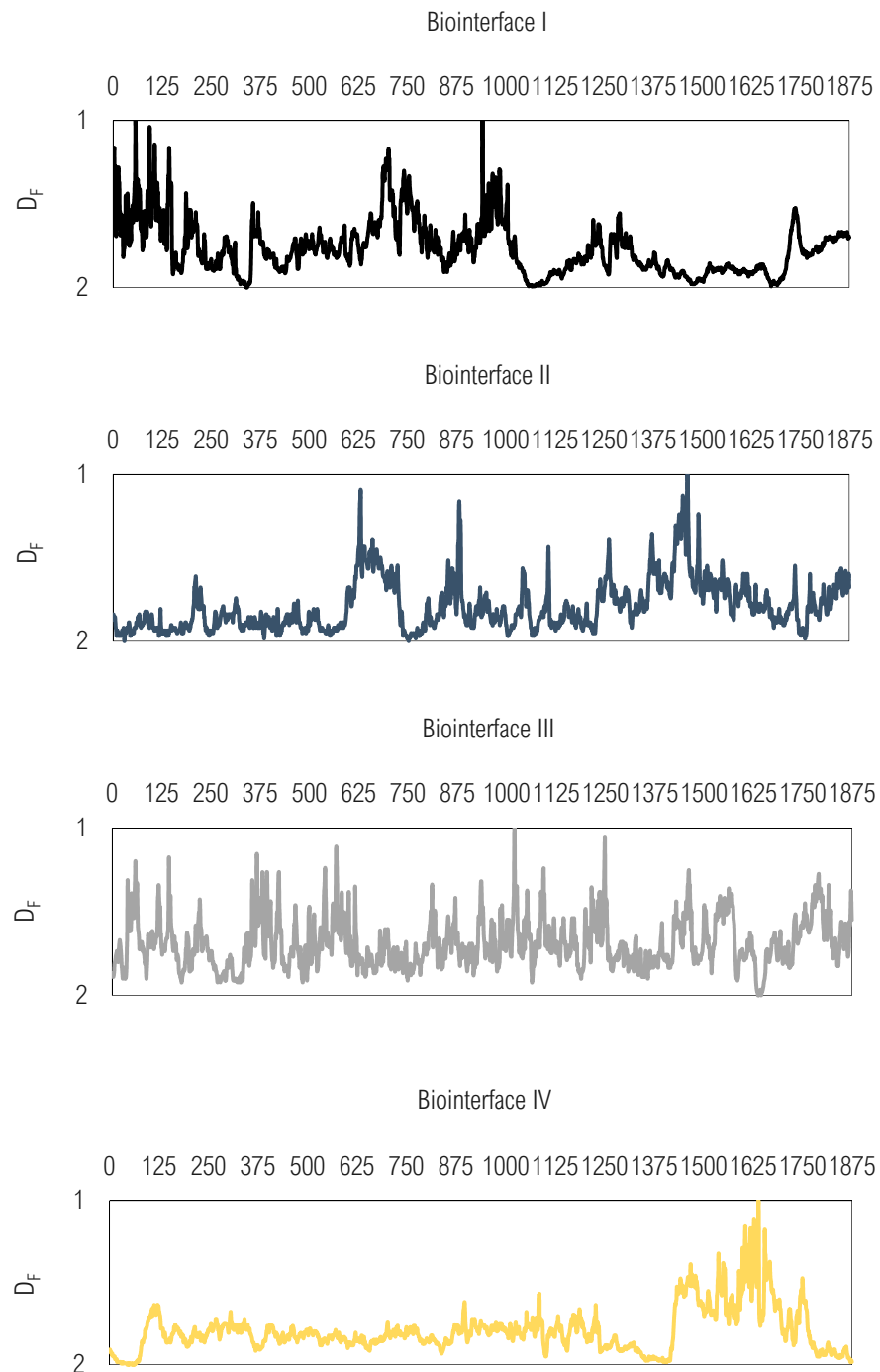


Figure 2. Cont.

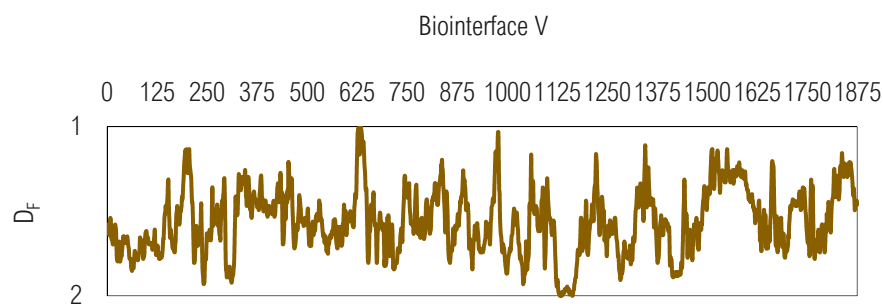


Figure 2. Photogrammetric distribution of fractal microcracks on carbon-capturing biointerfaces from hydrochars of sugarcane bagasse (I), pinewood sawdust (II), peanut pod hull (III), wheat straw (IV) and peaty compost (V). The closer to 1 the D_F , the smoother the pattern. By contrast, the closer from 2 the D_F the rougher the pattern.

Plainly, fractality depended on typology of feedstock for making hydrochar into an adsorbent (Figure 2). Thereby, inter-quartile range (Q_{75} – Q_{25}) of D_F was 1.40–1.70 for the biointerface V (peaty compost), making it the smoothest and most homogeneous high-throughput carbon-capturing framework. Another smoother bioproduct referred to biointerface III (peanut pod shell) by developing microstructural stresses with D_F of 1.60–1.795. By contrast, lower (Q_{25}) and upper (Q_{75}) quartiles of D_F were, respectively, 1.75 and 1.85 for the biointerface IV (wheat straw), making it the roughest and most heterogeneous biostructure by concentrating more points outside the range of “whiskers” in the box-plot (Figure 3). Additionally, sugarcane bagasse and pinewood sawdust developed topographically similar biointerfaces, with microcracks in the inter-quartile ranges of D_F of 1.695–1.895 and 1.70–1.90, respectively.

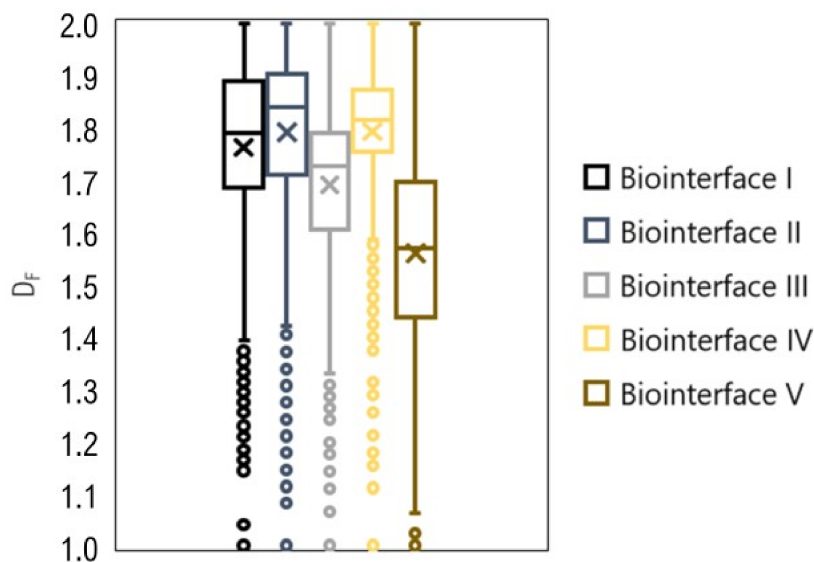


Figure 3. Heterogeneity of fractal mechanical stresses on carbon-capturing biointerfaces from hydrochars of sugarcane bagasse (I), pinewood sawdust (II), peanut pod hull (III), wheat straw (IV) and peaty compost (V). The larger the box, the more heterogeneous the surface. By contrast, the shorter the box, the more homogeneous the surface. Any point outside the range of “whiskers” is an indicator of non-random variability.

Overall, the imagery protocol we propose to analyze topographically irregular carbon-adsorbing frameworks proved useful to determine the fractality and how it could impact the functionality at the surface. Although we successfully harmonized stereomicroscopy, SLIC and BCM into a high-throughput protocol, it consumed an appreciable amount of

time to process samples and thus automation is necessary for overcoming the operational limitation to scale.

3.2. Potential Adsorption on Biointerfaces

All fractal biointerfaces proved useful for high-throughput adsorption (Table 2). However, biointerface V (peaty compost) most effectively adsorbed the CO₂. Hence, it outstripped the other potential physical sorbents in the process of capturing and binding molecules of adsorbate to pores and at functional sites on the surface. Biointerface V structured up the largest inherent pores and contained most gas-binding sites, namely N and S. In addition, it ended up “less fractally” in microstructural stresses and thus most resisted loss of functionality by mechanical deformation and absorption of environmental vapor during storage. Biointerfaces I (sugarcane bagasse) and III (peanut pod shell) encapsulated the CO₂ as effectively as the distinctive biointerface V, although they developed larger non-original irregularities and contained more O, which likely were characteristics of disordering at the surface. By contrast, biointerfaces II (pinewood sawdust) and IV (wheat straw) developed the largest fractal microcracks and therefore were the roughest on the finish surface. Mechanical stresses heavily penetrated through them and promoted critical breakpoints, hygroscopicity and, most importantly, losses of functional gas-binding alkaline sites (N and S) and matter (C). Since roughness destabilized the material, we could track significant negative correlations between D_F and μ ($r = -0.75$), C ($r = -0.85$), N ($r = -0.90$), S ($r = -0.95$), however, a significant positive correlation with H_{yg} ($r = 0.95$) (Table S3, Supplementary Material).

Table 2. Static adsorption and physicochemical properties of biointerfaces.

Property	Biointerface				
	I	II	III	IV	V
Static adsorption [mmol CO ₂ g ⁻¹]	8.20	7.45	8.35	7.10	8.65
Surfac area [m ² g ⁻¹]	98.10	97.95	103.80	88.35	105.40
Width of pore [nm]	1.20	1.05	1.60	1.10	1.65
Diameter of pore [nm]	1.80	1.65	2.20	1.35	2.25
Volume of pore [m ³ g ⁻¹]	70.05	60.80	95.10	55.40	105.60
C [%]	46.70	45.20	50.20	38.40	54.10
O [%]	42.95	39.80	46.75	48.10	44.90
N [%]	0.10	0.10	0.15	0.05	0.20
S [%]	0.05	0.05	0.10	0.05	0.20
Hygroscopicity [%]	8.10	8.35	7.80	9.50	5.45
Durability [%]	97.90	96.60	98.05	97.05	99.10
Fractal dimension of microstructural stress	1.75	1.75	1.70	1.80	1.55

Sugarcane bagasse (I), pinewood sawdust (II), peanut pod hull (III), wheat straw (IV) and peaty compost (V).

3.3. Adsorption-Fractality Nexus

The sigmoid Gompertz function adequately predicted the adsorption upon fractality of microstructural stresses on carbon-capturing biointerfaces (Figure 4). Since biointerface V (peaty compost) developed the smoothest and most homogeneous surface, it is associated with the most gradual breakthrough curves in physicochemical losses of C, N and S, and adsorption. Thereby, we could estimate (Table S4, Supplementary Material) the lowest value for the shape-parameter k to μ of biointerface V, further supporting its distinct behavior. Most notably, revealing how the magnitude of fractal stress could negatively impact the adsorption by decreasing availability of functional alkaline sites for the adsorbate to have contact with the surface.

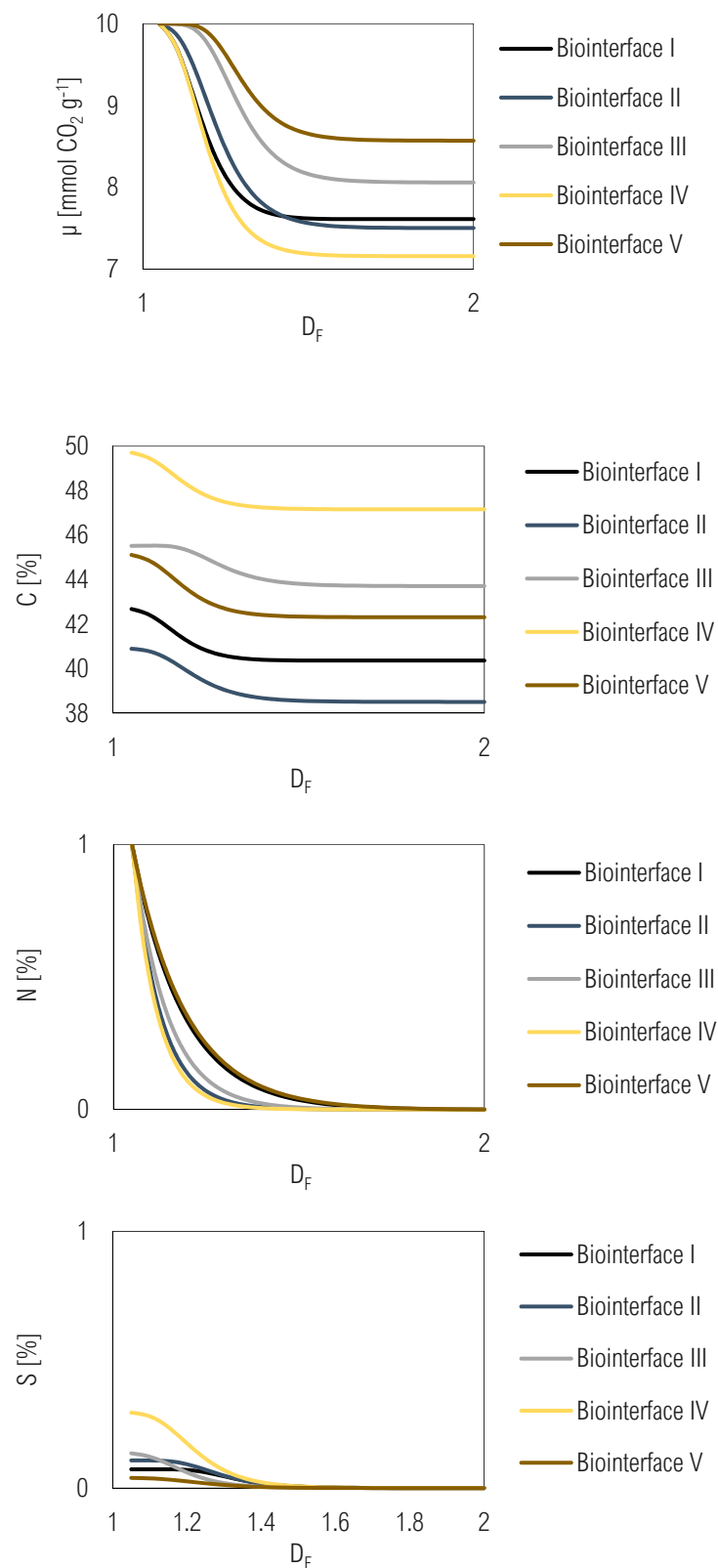


Figure 4. Functional relationships between adsorption, functionality and fractality of bioterfaces from hydrochars of sugarcane bagasse (I), pinewood sawdust (II), peanut pod hull (III), wheat straw (IV) and peaty compost (V) at sigmoid Gompertz function.

The flatter the curve, the less probable the material is to a functionality-limiting fractality. By contrast, the steeper the curve, the more probable the fractal stress is to

disorder the function of an adsorbent. We could capture the limitation of rougher fractals to functionality into estimates of $\beta > 1$ for N. A $\beta \geq 1$ accelerates the relative decrease in functionality with irregularity. By contrast, $\beta < 1$ decelerates the relative decrease, while the expectation for $\beta = 1$ is to keep it constant. Largest values for both β (2.75×10^{-4}) and k (-6.35) for the S on biointerface IV (wheat straw) validated the importance of avoiding fractals as large as 1.70–1.90 for an adsorbent to properly function.

Overall, we could decide 1.40 as the limit of D_F of power-law microstructural stresses to develop high-throughput carbon-capturing frameworks, capable of 8.65 mmol g^{-1} . Any value above 1.40 could not change the functionality. However, Gompertz model always has the limitation of not fitting for the stationary region of a sigmoidal dynamics.

3.4. Cross-Validation of Protocol

The PCA robustly divided the high-dimensionality dataset into useful subsets (Table S5, Supplementary Material). The orthogonal latent hits, namely PC_I and PC_{II} , together explained about 90% of variability in functionality–fractality nexus of biointerfaces capable of adsorption and chemisorption of CO_2 . The PC_I (bifunctionality) had significant positive correlations with μ ($r = 0.90$), S_A ($r = 0.90$), W_P ($r = 0.95$), D_P ($r = 0.90$), V_P ($r = 0.95$), C ($r = 0.95$), N ($r = 0.95$), S ($r = 0.90$) and durability ($r = 0.90$), however, significant negative correlations with O ($r = -0.95$) and D_F ($r = -0.95$). The D_F and H_{yg} moved towards the left-lower and left-upper quadrants in the bi-plot chart, respectively, closest to structuration of lowest-intensity pixels (Figure 5; Figure S2, Supplementary Material). Therefore, the larger the non-Euclidean failure on the surface the lower the intensity of pixel, and thus the more likely the biointerface is to not properly function. Biointerface V (peaty compost) most concentrated high-intensity pixels in 2D plane, according to its distinct capability to adsorb CO_2 . Complementarily, PC_{II} (disordering at the surface) had a single significant positive correlation with O ($r = 0.95$). The O moved towards the right-upper quadrant in the factorial map, closest to low-intensity pixels outside the interquartile range of D_F . Therefore, the more topographically irregular and heterogeneous the surface the higher the content of O, as the larger the loss of hetero atoms of N and S. Biointerface IV (wheat straw) produced more low-intensity and medium-intensity pixels than any other biomaterial, which were characteristics of rougher and more oxygenated adsorbent with lower durability and not capable of performing an effective adsorption. Plainly, an atypical oxygenation in biointerface IV disordered its potential adsorption.

4. Discussion

We created an imagery protocol to predict adsorption in the fractal dimension of microstructural stresses. Most notably, we validated it by analyzing carbon-capturing biointerfaces. The protocol of high-resolution stereomicroscopy can be useful to capture outstanding chromatic contrast at biosurfaces and generate sufficient imagery data in micrographs to determine the D_F on BCM after pixel-wise segmentation and quantization. The SLIC algorithm can perform an excellent oversegmentation by color or hue similarity and topological proximity in 2D plane, and thus enable the BCM to adequately determine the D_F of irregular microtopographies on digital biosurfaces. The outputs of BCM are accurate inputs to describe on sigmoid Gompertz function the dynamics between fractality and adsorbent's overall quality. Our approach is self-sustaining and could compensate for the complexities of traditionally determining the D_F in sorption analyzer or thermogravimetric equipment. The user can quantitatively analyze adsorbents easily and, potentially, save some amount of time pre-processing samples to improve imagery data quality. Another advantage, relative to the existing literature [12,23], is the independence from private analytical softwares. The R-project is an open-sourcing programming language and supports cutting edge computer vision. Disadvantages of our concept are few. However, snapshotting could be time-consuming, which emphasizes the necessity of automation before resembling conditions on an industrial scale. Another direction for future studies of the soundness of our preliminary yet exciting approach is to analyze it economically.

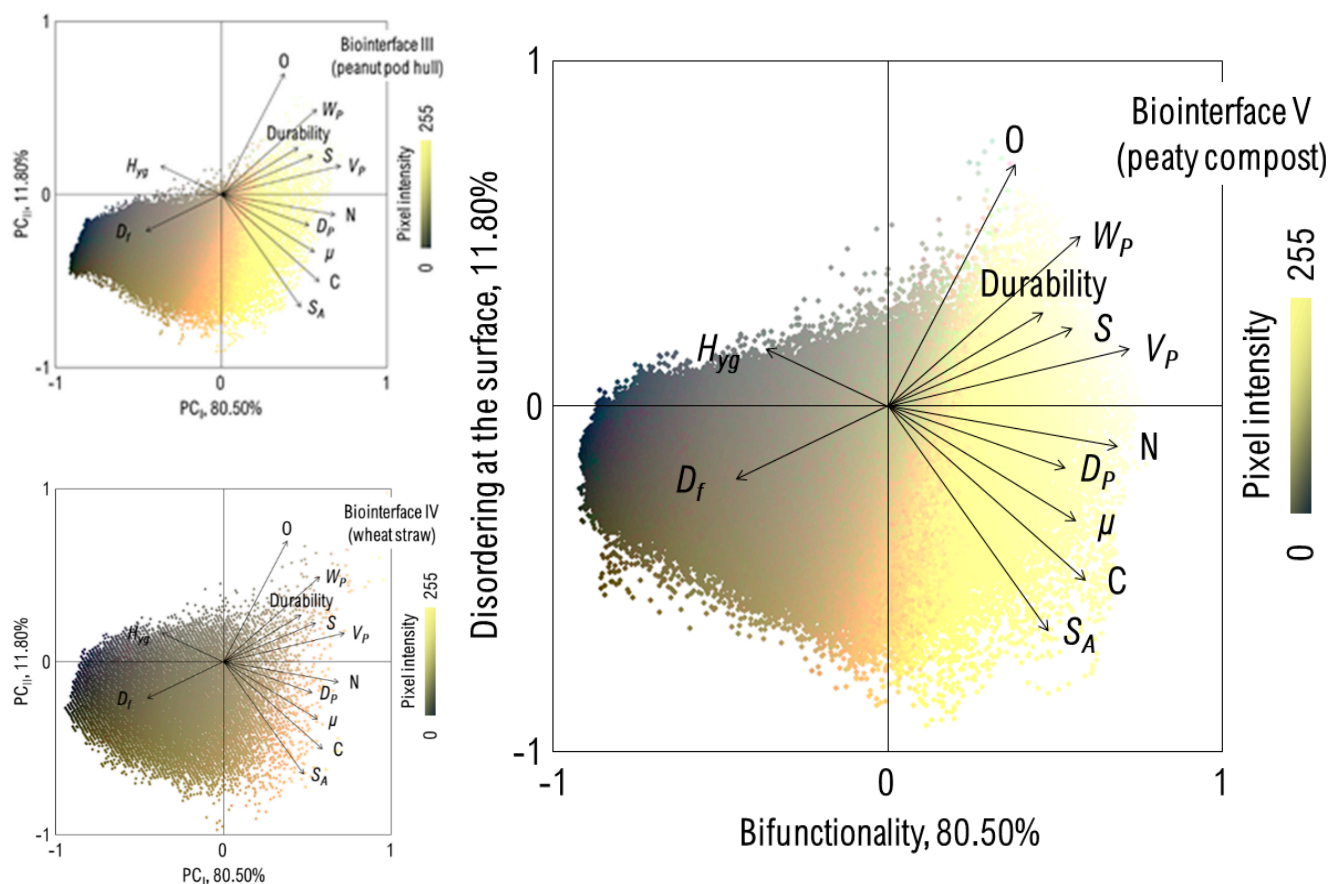


Figure 5. Functionality-fractality nexus. The factorial diagram predicts the functionality upon imagery data. For instance, the lower the intensity of pixel the rougher the mechanical stress, and thus the more intensive the loss of structural pores and functional sites to an effective capturing and binding of CO_2 on the surface of the material.

Biointerface V can distinctly develop “less fractally” mechanical stresses, preserving most of its original physics and chemistry of surface to support an effective capturing and binding of acidic CO_2 in pores and at alkaline functional sites. If D_f is larger than 1.40, which corresponds to power-law stresses on the highest carbon-capturing biointerface, fractal microcracks can promote significant physical and chemical losses, considerably declining adsorption. If not, underperformance is not likely. Similar studies on gas-adsorbing biocarbons are often not available from the typical literature, making it challenging for contrasting our trends. However, we can read into a few examples where the larger either pore or edge of fractal dimension, the higher the adsorption [19,25], supporting the outperformance of biointerface V. Peaty compost can develop larger and more regular pores, relative to other raw materials. Hence, it is the most reliable option to convert low-pressure powders into high-performance carbon-capturing frameworks. Another potential option to develop high-performance physical biosorbents would be peanut pod hull. Recycling or re-use of both peaty compost and peanut pod hull could create conditions for promoting carbon-to-waste paths across plans to green chemistry, circular economy and net zero society. Biointerfaces could replace fossil fuels in adsorption, potentially improving its environmental footprint. Thus, further in-depth investigations must focus on LCA for assessing if it would be possible for our approach to reduce environmental impacts of developing adsorbents towards CCS and CCU platforms.

Sigmoid Gompertz function and PCA can be of great assistance to accurately predict how the magnitude and distribution of fractals on the surface can impact the characteristics of both imagery protocol and product. Sridhar et al. [38] harmonized the features of

adsorption and fractality of pores. Yet, our study can bring innovation in extracting useful statistics from non-Euclidean geometries non-inherent to the biomaterial to describe the destabilization of pore network architecture, hetero atoms of N and S, and hydrophobicity. Ren et al. [24] stressed the capacity of an atypical hygroscopicity to destroy functional sites on the surface, thereby reducing adsorption, in agreement with the negative correlations between D_F , μ and H_{yg} . Larger fractals can make it easier for the surface to uptake water, reducing adsorption by promoting either aging on pores and physicochemical functional sites or further structural damage. An indicative of disordering at the surface is an accentuated concentration of O, which is predictable by orthogonalizing lower-intensity pixels in micrographs. An atypical oxygenation is attributable to rougher microcracks at the level of adsorbent or, correspondently, lower-intensity pixels at the level of scanning.

5. Conclusions

Our study introduces a high-throughput imagery protocol to analyze functionality upon fractality of carbon-capturing biointerfaces. By integrating image processing and fractal analytics, we are able to obtain typical micrographs to determine the fractality of microstructural stress and how it impacts the functionality of an adsorbent. The larger the fractal dimension of an atypical irregularity on the surface, the lower the potential physical sorption, as the loss of functional gas-binding sites and matter occurs. Our insights are timely and serve as a springboard of developing cutting edge analytical methods of adsorption. In addition, carbon-capturing biointerfaces act as an opening for eco-compatible solutions to progress in the field's prominence in evolving CCS and CCU platforms towards mitigating global warming without negatively impacting on the society and environment.

Supplementary Materials: The following supporting information can be downloaded at: <https://www.mdpi.com/article/10.3390/agronomy12020446/s1>, Figure S1: Bibliometric network on the specific topic of 'applying fractals to adsorption' (Elsevier's Scopus and Clarivate's Web of Sciences on 1 December 2021); Figure S2: Functional relationship between properties of fractal carbon-capturing biointerfaces and pixel-wise stereomicroscopy imagery data; Table S1: Specifications of digital autoclave; Table S2: Specifications of automatic pelletizer; Table S3: Spearman matrix for relationships between properties of fractal carbon-capturing biointerfaces; Table S4: Parametrization and adequacy of sigmoid Gompertz function for adsorption of CO₂ on fractal biointerfaces; Table S5: Principal components into the adsorption-fractality nexus.

Author Contributions: Conceptualization, B.R.d.A.M.; methodology, B.R.d.A.M.; formal analysis, B.R.d.A.M.; investigation, B.R.d.A.M., A.L.d.B.F. and M.R.B.J.; data curation, B.R.d.A.M.; writing—original draft preparation, B.R.d.A.M.; writing—review and editing, B.R.d.A.M., A.L.d.B.F. and M.R.B.J.; visualization, B.R.d.A.M., A.L.d.B.F., M.R.B.J. and R.P.d.S.; supervision, R.P.d.S.; project administration, R.P.d.S.; funding acquisition, R.P.d.S. All authors have read and agreed to the published version of the manuscript.

Funding: This research was funded by Coordination for the Improvement of Higher Education Personnel (CAPES, financing code 001) and Coordination of the Graduate Program in Agronomy, Plant Production (FCAV/Unesp).

Institutional Review Board Statement: Not applicable.

Informed Consent Statement: Not applicable.

Data Availability Statement: The data that support the findings of this study are available on request from the corresponding author, B.R.d.A.M.

Conflicts of Interest: The authors declare no potential conflict of interest.

Abbreviations

μ	adsorption [mmol CO ₂ g ⁻¹]
AFM	atomic force microscopy
BCM	box-counting method
C	elemental carbon [%]
CCS	carbon capture and storage
CCU	carbon capture and utilization
D_F	fractal dimension
D_p	diameter of pore [nm]
EDS	energy-dispersive X-ray spectrometry
FSEM	field emission scanning electron microscopy
FPS	frames per second
HTC	hydrothermal carbonization
H_{yg}	hygroscopicity [%]
IPCC	Intergovernmental Panel on Climate Change
KMO	Kaiser-Meyer-Olkin
LCA	life cycle analysis
N	elemental nitrogen [%]
PCA	principal component analysis
PC _I	primary principal component
PC _{II}	secondary principal component
PNG	portable network graphic
S	elemental sulfur [%]
S_A	surface area [m ² g ⁻¹]
SANS	small-angle neutron scattering
SAXS	small-angle X-ray scattering
SEM	scanning electron microscopy
SLIC	simple linear iterative clustering
TEM	transmission electron microscopy
V_P	volume of pore [m ³ g ⁻¹]
W_P	width of pore [nm]

References

1. Masson-Delmotte, V.P.; Zhai, A.; Pirani, S.L.; Connors, C.; Péan, S.; Berger, N.; Caud, Y.; Chen, L.; Goldfarb, M.I.; Gomis, M.; et al. (Eds.) *Sixth Assessment Report Climate Change 2021: The Physical Science Basis—A Report of Working Group I to the Sixth Assessment Report of the Intergovernmental Panel on Climate Change*; IPCC: Geneva, Switzerland, 2021.
2. Warudkar, S.S.; Cox, K.R.; Wong, M.S.; Hirasaki, G.J. Influence of stripper operating parameters on the performance of amine absorption systems for post-combustion carbon capture: Part, I. High pressure strippers. *Int. J. Greenh. Gas. Control.* **2013**, *16*, 342–350. [[CrossRef](#)]
3. Trickett, C.A.; Helal, A.; Al-Maythaly, B.A.; Yamani, Z.H.; Cordova, K.E.; Yaghi, O.M. The chemistry of metal–organic frameworks for CO₂ capture, regeneration and conversion. *Nat. Rev. Mater.* **2017**, *2*, 17045. [[CrossRef](#)]
4. Minelli, M.; Papa, E.; Medri, V.; Miccio, F.; Benito, P.; Doghieri, F.; Landi, E. Characterization of novel geopolymer–Zeolite composites as solid adsorbents for CO₂ capture. *Chem. Eng. J.* **2018**, *341*, 505–515. [[CrossRef](#)]
5. Coenen, K.; Gallucci, F.; Hensen, E.; van Sint Annaland, M. Kinetic model for adsorption and desorption of H₂O and CO₂ on hydrotalcite-based adsorbents. *Chem. Eng. J.* **2019**, *355*, 520–531. [[CrossRef](#)]
6. Kacem, M.; Pellerano, M.; Delebarre, A. Pressure swing adsorption for CO₂/N₂ and CO₂/CH₄ separation: Comparison between activated carbons and zeolites performances. *Fuel Process. Technol.* **2015**, *138*, 271–283. [[CrossRef](#)]
7. Lillia, S.; Bonalumi, D.; Fosbøl, P.L.; Thomsen, K.; Jayaweera, I.; Valenti, G. Thermodynamic and kinetic properties of NH₃-K₂CO₃-CO₂-H₂O system for carbon capture applications. *Int. J. Greenh. Gas Control* **2019**, *85*, 121–131. [[CrossRef](#)]
8. Igalavithana, A.D.; Kim, K.-H.; Jung, J.-M.; Heo, H.-S.; Kwon, E.E.; Tack, F.M.G.; Tsang, D.; Jeon, Y.J.; Ok, Y.S. Effect of biochars pyrolyzed in N₂ and CO₂, and feedstock on microbial community in metal(loid)s contaminated soils. *Environ. Int.* **2019**, *126*, 791–801. [[CrossRef](#)] [[PubMed](#)]
9. Sultan, U.; Zhang, Y.; Farooq, M.; Imran, M.; Khan, A.A.; Zhuge, W.; Khan, T.A.; Yousaf, M.H.; Ali, Q. Qualitative assessment and global mapping of supercritical CO₂ power cycle technology. *Sustain. Energy Technol. Assess.* **2021**, *43*, 100978. [[CrossRef](#)]
10. Godin, J.; Liu, W.; Ren, S.; Xu, C.C. Advances in recovery and utilization of carbon dioxide: A brief review. *J. Environ. Chem. Eng.* **2021**, *9*, 105644. [[CrossRef](#)]
11. Siddiqui, M.A.Q.; Ueda, K.; Komatsu, H.; Shimamoto, T.; Roshan, H. Caveats of using fractal analysis for clay rich pore systems. *J. Pet. Sci. Eng.* **2020**, *195*, 107622. [[CrossRef](#)]

12. Li, C.; Hao, M.; Geng, Z.; He, Y.; Wei, S. Drop-weight impact fragmentation of gas-containing coal particles. *Particuology* **2021**, *55*, 35–42. [CrossRef]
13. Jiang, G.; Cai, L.; Wang, S.; Laaksonen, A.; Feng, X.; Mu, L.; Lu, X.; Zhu, J. Critical role of carbonized cellulose in the evolution of highly porous biocarbon: Seeing the structural and compositional changes of spent mushroom substrate by deconvoluted thermogravimetric analysis. *Ind. Eng. Chem. Res.* **2020**, *59*, 22541–22548. [CrossRef]
14. Ossler, F.; Santodonato, L.J.; Bilheux, H.Z. In-situ neutron imaging of hydrogenous fuels in combustion generated porous carbons under dynamic and steady state pressure conditions. *Carbon* **2017**, *116*, 766–776. [CrossRef]
15. Geng, Z.; Xiao, Q.; Lv, H.; Li, B.; Wu, H.; Lu, Y.; Zhang, C. One-step synthesis of microporous carbon monoliths derived from biomass with high nitrogen doping content for highly selective CO₂ capture. *Sci. Rep.* **2016**, *6*, 30049. [CrossRef]
16. Cai, J.; Lin, D.; Singh, H.; Wei, W.; Zhou, S. Shale gas transport model in 3D fractal porous media with variable pore sizes. *Mar. Pet. Geol.* **2018**, *98*, 437–447. [CrossRef]
17. Zhang, R.-H.; Wu, J.-F.; Zhao, Y.-L.; He, X.; Wang, R.-H. Numerical simulation of the feasibility of supercritical CO₂ storage and enhanced shale gas recovery considering complex fracture networks. *J. Pet. Sci. Eng.* **2021**, *204*, 108671. [CrossRef]
18. He, H.; Liu, P.; Xu, L.; Hao, S.; Qiu, X.; Shan, C.; Zhou, Y. Pore structure representations based on nitrogen adsorption experiments and an FHH fractal model: Case study of the block Z shales in the Ordos Basin, China. *J. Pet. Sci. Eng.* **2021**, *203*, 108661. [CrossRef]
19. Zhang, L.; Cao, S.; Li, Z.; Zhang, H.; Duan, F. Pore structure of sludge char and simultaneously NO removal characteristics in the treated flue gas from Ca-L. *Fuel* **2021**, *289*, 119937. [CrossRef]
20. Xiang, G.; Ye, W.; Yu, F.; Wang, Y.; Fang, Y. Surface fractal dimension of bentonite affected by long-term corrosion in alkaline solution. *Appl. Clay Sci.* **2019**, *175*, 94–101. [CrossRef]
21. Feng, Y.; Li, Y.; Wang, J.; Wu, M.; Fan, H.; Mi, J. Insights to the microwave effect in the preparation of sorbent for H₂S removal: Desulfurization kinetics and characterization. *Fuel* **2017**, *203*, 233–243. [CrossRef]
22. Li, Z.; Liu, D.; Cai, Y.; Wang, Y.; Teng, J. Adsorption pore structure and its fractal characteristics of coals by N₂ adsorption/desorption and FESEM image analyses. *Fuel* **2019**, *257*, 116031. [CrossRef]
23. Wen, H.; Wei, G.; Ma, L.; Li, Z.; Lei, C.; Hao, J. Damage characteristics of coal microstructure with liquid CO₂ freezing-thawing. *Fuel* **2019**, *249*, 169–177. [CrossRef]
24. Ren, Q.; Zhang, Y.; Arauzo, I.; Shan, L.; Xu, J.; Wang, Y.; Su, S.; Hu, S.; Xiang, J. Roles of moisture and cyclic loading in microstructures and their effects on mechanical properties for typical Chinese bituminous coals. *Fuel* **2021**, *293*, 120408. [CrossRef]
25. Lin, K.; Huang, X.; Zhao, Y.-P. Combining image recognition and simulation to reproduce the adsorption/desorption behaviors of shale gas. *Energy Fuels* **2020**, *34*, 258–269. [CrossRef]
26. Panigrahi, S.; Sharma, H.B.; Dubey, B.K. Overcoming yard waste recalcitrance through four different liquid hot water pretreatment techniques—Structural evolution, biogas production and energy balance. *Biomass Bioenergy* **2019**, *127*, 105268. [CrossRef]
27. Iftikhar, M.; Asghar, A.; Ramzan, N.; Sajjadi, B.; Chen, W.-Y. Biomass densification: Effect of cow dung on the physicochemical properties of wheat straw and rice husk based biomass pellets. *Biomass Bioenergy* **2019**, *122*, 1–16. [CrossRef]
28. Sharma, H.B.; Dubey, B.K. Co-hydrothermal carbonization of food waste with yard waste for solid biofuel production: Hydrochar characterization and its pelletization. *Waste Manag.* **2020**, *118*, 521–533. [CrossRef] [PubMed]
29. Whittaker, C.; Shield, I. Factors affecting wood, energy grass and straw pellet durability—A review. *Renew. Sustain. Energy Rev.* **2017**, *71*, 1–11. [CrossRef]
30. Goel, C.; Kaur, H.; Bhunia, H.; Bajpai, P.K. Carbon dioxide adsorption on nitrogen enriched carbon adsorbents: Experimental, kinetics, isothermal and thermodynamic studies. *J. CO₂ Util.* **2016**, *16*, 50–63. [CrossRef]
31. Gargiulo, V.; Gomis-Berenguer, A.; Giudicianni, P.; Ania, C.O.; Ragucci, R.; Alfè, M. Assessing the potential of biochars prepared by steam-assisted slow pyrolysis for CO₂ adsorption and separation. *Energy Fuels* **2018**, *32*, 10218–10227. [CrossRef]
32. Abdulmumini, M.M.; Zigan, S.; Bradley, M.S.; Lestander, T.A. Fuel pellet breakage in pneumatic transport and durability tests. *Renew. Energy* **2020**, *157*, 911–919. [CrossRef]
33. Sigvardsen, N.M.; Ottosen, L.M. Characterization of coal bio ash from wood pellets and low-alkali coal fly ash and use as partial cement replacement in mortar. *Cem. Concr. Compos.* **2019**, *95*, 25–32. [CrossRef]
34. Panigrahy, C.; Seal, A.; Mahato, N.K.; Bhattacharjee, D. Differential box counting methods for estimating fractal dimension of gray-scale images: A survey. *Chaos Solitons Fractals* **2019**, *126*, 178–202. [CrossRef]
35. Tjørve, K.M.C.; Tjørve, E. The use of Gompertz models in growth analyses, and new Gompertz-model approach: An addition to the Unified-Richards family. *PLoS ONE* **2017**, *12*, e0178691. [CrossRef] [PubMed]
36. Migenda, N.; Möller, R.; Schenck, W. Adaptive dimensionality reduction for neural network-based online principal component analysis. *PLoS ONE* **2021**, *16*, e0248896. [CrossRef]
37. R Core Team. R: A Language and Environment for Statistical Computing. Available online: <http://www.R-project.org/> (accessed on 25 June 2021).
38. Sridhar, M.; Gunugunuri, K.; Hu, N.; Motahari, A.; Zuo, X.; Schaefer, D.W.; Thiel, S.W.; Smirniotis, P.G. Impact of interfacial roughness on the sorption properties of nanocast polymers. *Macromolecules* **2016**, *49*, 2663–2670. [CrossRef]